The native oxide skin of liquid metal Ga nanoparticles prevents their rapid coalescence during electrocatalysis

Valery Okatenko,[†] Laia Castilla-Amorós,[†] Dragos Stoian,[⊥] Jan Vávra,[†] Anna Loiudice,[†] Raffaella Buonsanti[†]*

[†]Laboratory of Nanochemistry for Energy Research, Institute of Chemical Sciences and Engineering, Ecole Politechnique Fédérale de Lausanne, Sion, CH-1950, Switzerland

[⊥]Swiss-Norwegian Beamlines, European Synchrotron Radiation Facility, 38000 Grenoble, France

*email: raffaella.buonsanti@epfl.ch

Abstract

Liquid metals (LMs) have been used in electrochemistry since the 19th century, but it is only recently that they have emerged as electrocatalysts with unique properties, such as inherent resistance to coke-poisoning, which derives from the dynamic nature of their surface. The use of LM nanoparticles (NPs) as electrocatalysts is highly desirable to enhance any surface-related phenomena. However, LM NPs are expected to rapidly coalesce, similarly to liquid drops, which makes their implementation in electrocatalysis hard to envision. Herein, we demonstrate that liquid Ga NPs drive the electrochemical CO_2 reduction reaction (CO_2RR) while remaining well-separated from each other. The combination of electrochemical, microscopic and spectroscopic techniques, including *operando* X-Ray absorption, indicates that the unique properties of the native oxide skin of the Ga NPs account for their resistance to coalescence during operation. This discovery provides an avenue for future development of Ga-based LM NPs as a new class of electrocatalysts.

Introduction

Liquid metals (LM) are unique materials which combine the low viscosity and good fluidity of liquids with the high thermal and electrical conductivity of metals.[1–7] Several metals possess melting points close to the room temperature, which include Cs (28.5 °C), Rb (39.3 °C), Hg

(−38.8 °C) and Ga at 29.8 °C.[1–6] For a long time, their use was mostly limited to Hg, as alkali metals are too reactive in their metallic state, and Ga gets passivated with an oxide skin which complicates its manipulation because of the adhesive properties of gallium oxide.[7] Hg electrodes were used in the electrochemical chloro-alkali process, thus supplying chlorine, hydrogen and sodium hydroxide to the entire chemistry and chemical engineering industry.[8] As a result of the growing concerns about Hg toxicity, the use of LMs steadily decreased over the following decades.[1–6]

Recently, the field of LMs has undergone a true renaissance, which has partly been driven by the increasing interest in wearable devices.[1–6] Most research has centered on Ga and its alloys due to their low toxicity and melting point.[1–4] These materials have also emerged as a new class of catalysts wherein the highly dynamic liquid surface offers greater flexibility compared to solid catalysts.[6,9–16] Most of the studies so far have focused on thermal catalysis, including dry reforming of methane and alkane dehydrogenation.[9–12] For example, Pd atoms popping up on the surface of liquid Ga in PdGa alloys were shown to be extremely selective for the dehydrogenation of alkane while being resistant to coke poisoning.[9] Applications of LM are emerging also in electrocatalysis.[13–16] In one example, metallic Ce nanoparticles (NPs) were stabilized within Ga droplets to promote the conversion of CO_2 to solid carbonaceous species without undergoing deactivation by the buildup of reaction products.[13] In a second example, a selectivity change from hydrogen evolution to selective CO_2 reduction was observed to follow the solid-liquid conversion of a Ga-Sn-In catalyst.[14]

Despite these exciting opportunities in catalysis, the aforementioned studies are mostly based on bulk LMs.[6,9–16] NPs are highly beneficial in heterogeneous catalysis as their high surface area maximizes the number of active sites per mass of material, and nanoscale effects, which improve activity or selectivity, can also emerge.[17,18] At the same time, NP catalysts tend to sinter, which requires the development of protection schemes, such as oxide coatings.[19,20] Because of their fluidity, LM NPs are expected to coalesce even more rapidly compared to solid NPs, which poses doubts regarding their utilization as catalysts.

One unique feature of Ga-based LMs is the presence of a native oxide skin surrounding their liquid metal core.[1–7] This oxide skin regulates the surface properties of the LMs, thus it is important for many of their applications.[1–7] If stable under reaction conditions, the native oxide will also play a crucial role in catalysis, especially when moving from bulk to NPs.[1–6,21,22] For example, in the context of photocatalysis, studies show that it contributes to charge separation as a semiconducting material.[21,22] More generally, it may possess catalytic activity on its own

or regulate the access of reactants to the liquid core while preventing the NP coalescence. However, very little attention has been given to the native oxide skin in the context of catalysis.[1–6]

In this work, we study Ga NPs as catalysts for the electrochemical CO_2 reduction (CO_2RR). We choose CO_2RR as a model reaction because of its importance towards establishing a carbon neutral society.[23,24] Furthermore, Ga can convert CO_2 to CO.[25,26] We show that the Ga NPs retain their size during CO_2RR. This finding is opposite to the intuitive expectation that liquid particles would coalesce into a larger drop when placed close to each other while applying the highly cathodic potential needed for CO_2RR, which is supposed to remove the native oxide skin. The combination of analytical electrochemistry, electron microscopy and *operando* X-Ray absorption spectroscopy reveals the unique behavior of the oxide skin which accounts for the observed resistance towards coalescence of liquid Ga NPs during CO_2RR.

Methods

Chemicals. Gallium (III) chloride ($GaCl_3$, 99.999 %), tris(dimethylamino)gallium (III) dimer ($Ga_2(NMe_2)_6$, 99.9 %) and di-*n*-octylamine ($C_{16}H_{35}N$ or DOA, 98 %) are purchased from ABCR. *n*-Butyllithium solution 2.7 M in heptane (*n*-BuLi), oleic acid ($C_{17}H_{33}CO_2H$ or OLAC, 90 %), 1-octadecene ($C_{18}H_{36}$ or ODE, 90 %), toluene (anhydrous, 99.8 %) and ethanol (anhydrous, 99.5 %) were purchased from Sigma-Aldrich. Potassium carbonate (K_2CO_3, 99+ %, ACS reagent) was obtained from Acros organics. DOA, ODE and OLAC were degassed and dried under a vacuum at 110 °C for 4 h, cooled to room temperature, and then transferred airless to the glove box. All syntheses were carried out under an inert atmosphere using anhydrous solvents and standard glovebox and Schlenk-line techniques. Post-synthetic purification ("washing"), ligand exchange, handling, and storage of the as-synthesized materials were also carried out under inert atmosphere.

Material synthesis. 26 nm Ga NPs were synthesized by following a previously reported procedure.[27,28] 7 mL of ODE were loaded into a 25 mL three-necked flask equipped with a reflux condenser and dried under vacuum at 110 °C for one hour. Then, the reaction flask was filled with N_2 and heated to 290 °C, followed by a rapid injection of a pre-prepared solution containing 50 mg of $Ga_2(NMe_2)_6$ and 2.3 mL of DOA in 3.8 mL of dried ODE with a 10 mL syringe. Right after the injection, the temperature dropped to 235 – 240 °C, and the solution color changed from yellow to dark grey after 30 s, which indicated the NP formation. The reaction flask was then quenched using an ice bath and cooled down to room temperature. At 50 °C, 0.04 mL of dried OLAC were injected, and the solution was left stirring for a few minutes. To purify Ga NPs and separate them from by-products and unreacted precursors, 15 mL of anhydrous ethanol were added, followed by centrifugation at 5000 rpm for 20 min. After supernatant disposal, the Ga NPs were redispersed in anhydrous toluene, and the purification/precipitation step was repeated once more with addition of 0.1 mL of OLAC. The Ga NPs were stored in anhydrous toluene.

Material characterization. Transmission electron microscopy (TEM) images of Ga NPs were acquired on a Thermo-Fisher Tecnai-Spirit at 120 kV. 5 μL of as-synthesized Ga NPs were drop-casted on a carbon coated copper TEM grid (Ted Pella, Inc.) to prepare the sample for imaging. Particle size distribution was evaluated with the use of ImageJ software from datasets of at least 200 particles each.

TEM imaging with energy dispersive X-ray spectroscopy (EDXS) was performed on a Thermo-Fisher Tecnai Osiris TEM in scanning mode at an accelerating voltage of 200 kV. The

microscope is equipped with a high brightness X-FEG gun, silicon drift Super-X EDXS detectors and Bruker Esprit acquisition software.

Cryo-TEM heating experiments were performed on Thermo-Fisher Talos F200s at 200 kV with Gatan Sci. temperature control holder cooled with liquid nitrogen. The specimen was heated by resistive elements to the preset temperature.

Scanning electron microscopy (SEM) images were acquired with Thermo-Fisher Teneo using an in-lens (Trinity) detector at beam energy of 5 keV and current of 25 pA. Samples were imaged on conductive glassy carbon substrates used as electrodes for CO_2RR measurements.

X-Ray photoelectron spectroscopy (XPS) was performed by using an Axis Supra (Kratos Analyical) instrument using the monochromated Kα X-ray line of an Al anode. The pass energy was set to 40 eV with a step size of 0.15 eV. The samples were electrically insulated from the sample holder, and charges were compensated. Ga NP samples were prepared by drop-casting films onto clean glassy carbon substrates. The same substrates were used in electrochemical experiments. XPS fitting was performed in CasaXPS software. All data were referenced to the principal C 1s peak at 284.8 eV after fitting. In the Ga 2p region, only the Ga $2p_{3/2}$ peaks were used for fitting and quantification. In the Ga 3d region, both Ga-metal and Ga-oxide peaks were fitted with contributions from spin–orbit coupling; the Ga $3d_{3/2}$ and Ga $3d_{5/2}$ peak separations were fixed at 0.46 eV, and the relative intensities were fixed at 0.633. In general, all peaks from a particular region were first fitted with equal line widths, and then this constraint was relaxed to refine the fit.

Attenuated Total Reflectance (ATR) – Fourier Transform Infrared Spectroscopy (FTIR) was performed with a PerkinElmer Spectrum 100 instrument by covering the ATR window Ga NPs drop-casted on glassy carbon surface (10 μg of 18 nm Ga NPs on circular area of 1.33 cm^2). Air was used as a background measurement, and spectra were recorded with resolution of 0.5 cm^{-1}.

The Ga solution concentration was determined by Inductively Coupled Plasma Optical Emission Spectrometry (ICP-OES) performed on an Agilent 5100 device with a VistaChip II CCD detector. Each sample aliquot (20 μl) was first dried, then digested overnight in 142.5 μL of 70 % HNO_3 ICP grade solution and finally diluted with Milli-Q water to obtain the 2 wt. % acid content needed for the analysis. ICP grade Ga standard solution (1000 ppm in 2 wt. % HNO_3) was diluted with 2 wt. % HNO_3 to get fresh standards before each analysis used to create the calibration plot employed to determine the concentration of the sample solutions.

Electrode preparation. Glassy carbon plates (2.5 cm × 2.5 cm × 0.3 cm, Sigradur G, HTW) coated with electrocatalyst were used as the working electrode. Before coating, the glassy carbon plates were cleaned by consecutive ultrasonication in acetone, isopropanol and water for 10 min each to remove adsorbed contaminants of different nature. After this, the glassy carbon plates were polished using an alumina paste (50 nm alumina, BAS Inc.) on a polishing pad. Then, the substrates were sonicated in Milli-Q water for another 10 min, polished again on the pad free of alumina to make sure that alumina was removed and, finally, the glassy carbon plate was blown dry with N_2. The working electrodes (cathodes) were prepared by drop-casting 15 μg of Ga NPs in 14 μL of toluene onto a circular area of 1.33 cm^2 on the glassy carbon plates. To do so, Ga NPs stock solution aliquot was centrifuged for 10 min at 13300 rpm, then the supernatant was disposed and, finally, Ga NPs precipitate was re-dispersed in 14 μL of anhydrous toluene (the material was kept under protective N_2 atmosphere during all manipulations). No binder (e.g. Nafion) was added to the catalyst, as NP electrode films prepared as described do not detach from the electrode surface during the measurement and provide sufficient electric conductivity under CO_2RR conditions. After drop-casting, the electrodes were let to dry for 10-15 min, rinsed with ethanol to remove ligands and with water to remove excess of ethanol. The electrodes were blown dry with N_2 and tested as-prepared.

Electrodes for square-wave voltammetry (SWV) were prepared in the same way except that higher loading was used to obtain better signal and a different substrate was used. That is, a rod-shape 3.0 mm diameter (0.28 cm^2) glassy carbon electrode (MF-2012, Bioanalytical Systems, Inc.) was covered with 25 μg of Ga NPs or 125 μg of Ga MPs in 2 μL of toluene. For the tests of bulk Ga, a Ga pellet was placed in the custom J-shape electrode with bowl-like volume to prevent the loss of electric connection between liquid Ga and current collector because of Ga detachment. Electric current was supplied through a wire which was embedded into the plastic electrode body and kept isolated from the electrolyte.

Electrochemical measurements. All the electrochemical measurements were controlled with Biologic SP-300 potentiostat. Ambient pressure CO_2 electrolysis was carried out in a custom-made gas-tight electrochemical H-cell made of polycarbonate and fitted with Buna-N O-rings built in our laboratory. The electrochemical cell configuration provided parallel sitting of the working electrode with respect to the counter electrode to ensure a uniform potential distribution across the surface. Both working and counter electrodes exposed geometric surface area of 1.33 cm^2 limited by the O-rings. Catholyte and anolyte compartments were filled with 2 mL electrolyte each to concentrate liquid products and allow liquid products detection. A

Selemion AMV anion exchange membrane was used to separate the anodic and cathodic compartments and minimize reoxidation of CO_2RR products on the anode. Pt foil was used as the counter electrode, and Ag/AgCl electrode (leak free series) (Innovative Instruments, Inc.) was used as the reference electrode.

0.1 M $KHCO_3$ solution was used as electrolyte. To prepare such solution, 0.276 g of K_2CO_3 were diluted in 40 mL of Milli-Q water to obtain 0.05 M K_2CO_3 solution, which was bubbled for 30 min with CO_2 (99.999 %, Carbagas) prior to the start of measurements. During electrolysis, CO_2 was pre-humidified by passing its flow through a water bubbler and constantly supplied to both cell compartments via custom-made ceramic frits at a flow rate of 5 sccm each. With this, the gas was bubbled through the electrolyte to prevent CO_2 depletion, as well as to allow continuous analysis of gaseous products via a gas chromatograph. Mass flow controller (Bronkhorst) was used to control the flow rate of CO_2. For the experiments under N_2 atmosphere, the only difference was the gas source (N_2, 99.999 %, Carbagas); all the other details remained the same. The electrolysis experiments were performed in chronoamperometry mode.

Square-wave voltammetry was performed using the same potentiostat in the three-electrode glass cell under CO_2 atmosphere. Pt wire was used as counter electrode, and a Ag/AgCl electrode (MF-2056, Bioanalytical Systems, Inc.) was used as a reference electrode. The same 0.1 M $KHCO_3$ solution was used as electrolyte.

In both chronoamperometry and square-wave voltammetry tests, electrochemical impedance spectroscopy (EIS) was implemented prior to the main measurement to determine the electrochemical cell resistance (R_{cell}) and compensate for the ohmic losses. Four spectra were measured at the open-circuit potential, using 41 points between 1 MHz and 100 Hz, using a sinus amplitude of 20 mV and a pause time of 0.6 s between each frequency. Software utility in-built into the potentiostat software (EC-lab) was used to apply the ohmic loss correction to further measurement.

Products analysis. Gas chromatograph (GC, SRI instruments) equipped with a HayeSep D porous polymer column, thermal conductivity detector and flame ionization detector was used for the analysis of gaseous products. The GC was calibrated for H_2, CO, CH_4, C_2H_4 and C_2H_6, albeit only H_2 and CO were detected in this study. Five standard gas mixtures (Carbagas) were used to obtain the calibration plots for gaseous products concentrations determination. Ultra-high purity N_2 (99.999 %) was used as a carrier gas.

The Faradaic efficiency for the gaseous products is calculated with the following equation:

$$FE = \frac{n_e \times F \times C \times f \times P}{R \times T \times I}$$

where n_e is the number of electrons transferred to product formation; F is the Faraday constant (96485 C mol^{-1}); C is the measured concentration of the product by GC (in ppm); f is the gas flow rate (mL s^{-1}); P is the pressure (1.01×10^5 Pa); I is the imposed current (in A); R is the universal gas constant (8.314 J mol^{-1} K^{-1}) and T is the temperature (K). Values obtained after 10 min of electrolysis are not included in the calculation of Faradaic efficiency, as GC gas flow is not yet stabilized at that point.

The Faradaic efficiency of liquid products (in case of this study, only formate was detected) was determined in a similar manner. 0.25 mL of both the catholyte and the anolyte were collected and analyzed with high-performance liquid chromatography (HPLC) on UltiMate 3000 instrument from Thermo Scientific, which is equipped with Refractive Index Detector for products quantification and Aminex HPX-87H (BioRad) column for products separation (1 mM H$_2$SO$_4$ was used as eluent). The necessity to collect electrolyte from both compartments is reasoned by the possible products crossover from the catholyte to the anolyte compartment.

The resulting formula used for calculations of liquid products FE is:

$$FE = \frac{n_e \times F \times C}{V \times I \times t}$$

where n_e is the number of electrons transferred to product formation; F is the Faraday constant; C is the measured concentration of the product by HPLC (mol mL^{-1}); V is the cell volume (4 mL); I is the measured current (A); t is the duration of electrolysis (3600 s).

Electrode potential is recalculated with respect to RHE reference using iR compensation according to the equation:

$$E_{RHE} = E_{Ref} + 0.206 + 0.0591 \times pH - (R_{cell} \times I)$$

where E_{Ref} is the recorded potential against the Ag/AgCl reference electrode (V); +0.206 V is the Ag/AgCl reference electrode correction; R_{cell} is the ohmic resistance between the working and the reference electrode, which was defined using electrochemical impedance spectroscopy analysis prior to the measurement (Ohm); I is the imposed current (A).

For all values (FE, current density), error bars represent 95 % confidence intervals obtained with triplicate measurements. For derivative metrics (e.g. partial and normalized current densities), respective standard deviations were obtained according to the laws of error propagation.

***Operando* X-Ray absorption spectroscopy (XAS).** *Operando* XAS experiments were performed at the Swiss-Norwegian beamline (BM31) at the European Synchrotron Radiation

Facility (ESRF) in France. The electron preparation procedure was similar to that described earlier in this report, except that the catalyst was drop-casted onto thin (2.5 cm × 2.5 cm × 0.05 cm) glassy carbon support, and higher loading (60 μg for X-ray absorption near edge structure (XANES) and 80 μg for extended X-ray absorption fine structure (EXAFS) measurements) was used to achieve better signal quality.

The electrochemical cell implemented in the *operando* setup was as reported in the previous work performed in our group,[29,30] and reproduced the same H-cell used in the lab experiments but with Kapton window in the back of working electrode to allow the X-rays to pass through. This way, the experiment environment was as close to the in-house electrochemical testing as possible to allow *operando* material characterization. To obtain the reference spectra, metallic Ga film obtained by exfoliation of warm Ga pellet with Kapton tape and Ga_2O_3 diluted in boron nitride and shaped into the form of pellet were used. Reference spectrum obtained for metallic Ga with this approach yielded Ga-Ga distances representative of liquid Ga. Both transmission and fluorescence geometries yielded qualitatively similar spectra.

The *operando* measurements were carried out in fluorescence mode at an incident angle of approximately 45 degrees. The cell was aligned with a multi-use beamline fixation support, which permitted the cell alignment with respect to the incoming beam *via* an XYZ high-precision translation stage. A Si(111) double crystal monochromator (DCM) was used to condition the beam from the corresponding bending magnet. Fluorescence XANES and EXAFS spectra were acquired using a Vortex® one-element silicon drift detector (SDD) with XIA-Mercury digital electronics with a time-resolution of 40 sec per spectrum at Ga K-edge in XANES and 2 min per spectrum in EXAFS studies. Data extraction, normalization, and averaging were performed using the Demeter package (Athena and Artemis).[31]

Results and discussion

Materials synthesis and characterization.

Ga NPs were synthesized by means of colloidal chemistry, following a previously reported protocol.[27,28,32] This wet chemistry approach provides the uniform size distribution which is essential when investigating eventual size and morphology changes of the catalysts during operation. **Figure 1A** reports a representative transmission electron microscopy (TEM) image illustrating the uniformity of the Ga NPs which possess a diameter of 26 nm with the particles size distribution less than 10 % (**Figure S1**). Scanning transmission electron microscopy (STEM) imaging (**Figure 1B**) along with energy dispersive X-Ray spectroscopy (EDXS) elemental mapping of O and Ga and the line profile over one Ga NP (**Figure 1C-E**) evidence the presence of a native oxide skin around 2.6 nm thick on the Ga NPs, which is consistent with previous studies.[27,28,32]
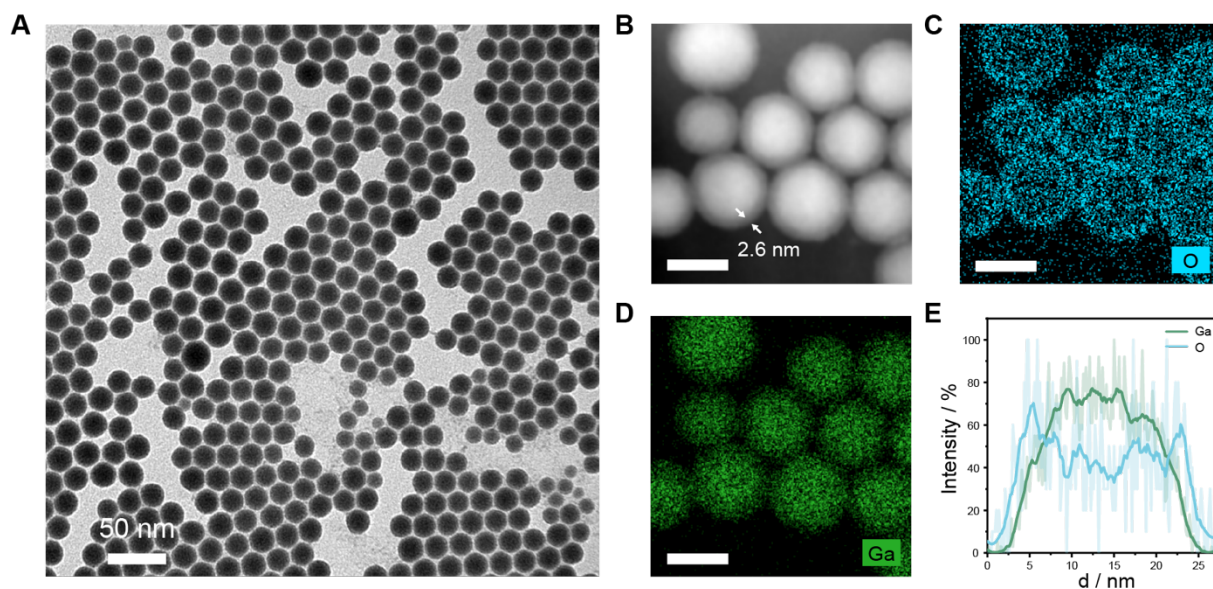

Figure 1. (A) Bright field TEM image of as-synthesized Ga NPs. (B-E) STEM characterization including (B) a typical image, (C, D) STEM-EDXS elemental mapping of Ga and O, respectively and (E) the line profile over one Ga NP, which confirm the presence of native oxide skin on as-synthesized Ga NPs (scale bar is 20 nm).

Electrochemical CO_2 reduction.

Bulk Ga electrodes were reported to be selective for CO_2RR with faradaic efficiency (FE) for CO of around 20%, the rest being H_2 from the competing hydrogen evolution reaction.[25]

We evaluated the catalytic performance of the Ga NPs to assess if they yielded a similar product distributions. First of all, the organic ligands were removed by ethanol rinsing before placing the electrode in the cell (**Figure S2**), in order to avoid their influence on the catalytic behavior. **Figure 2A** reports the CO FE measured over one hour of chronoamperometry at three different voltages, -0.7, -0.9 and -1.1 V_{RHE} (RHE = reversible hydrogen electrode), with the rest being H_2. At voltages more positive than -0.7 V_{RHE} the current density j is too low (**Figure S3**). Voltages which are more negative than -1.1 V_{RHE} result only in the increase of H_2 production. The selectivity of the Ga NPs varies with voltage. CO FE of Ga NPs is the highest at -0.7 V_{RHE} with an average value of 29 % (**Figure S4**). This value is slightly higher compared to that of bulk, which indicate possible size-dependent selectivity. As the voltage becomes more negative, CO FE decreases, and more H_2 is produced. In addition to CO and H_2, a minor amount of formate (<1 %) is detected at -1.1 V_{RHE}. With this products selectivity profile and CO_2 as carrier, the resulting gas mixture could be treated as H_2-rich syngas, which is a precursor for thermocatalytic dimethyl ether and methanol production.[33,34] **Figure 2B** confirms that the current density remains stable for one hour electrolysis without any major declining.
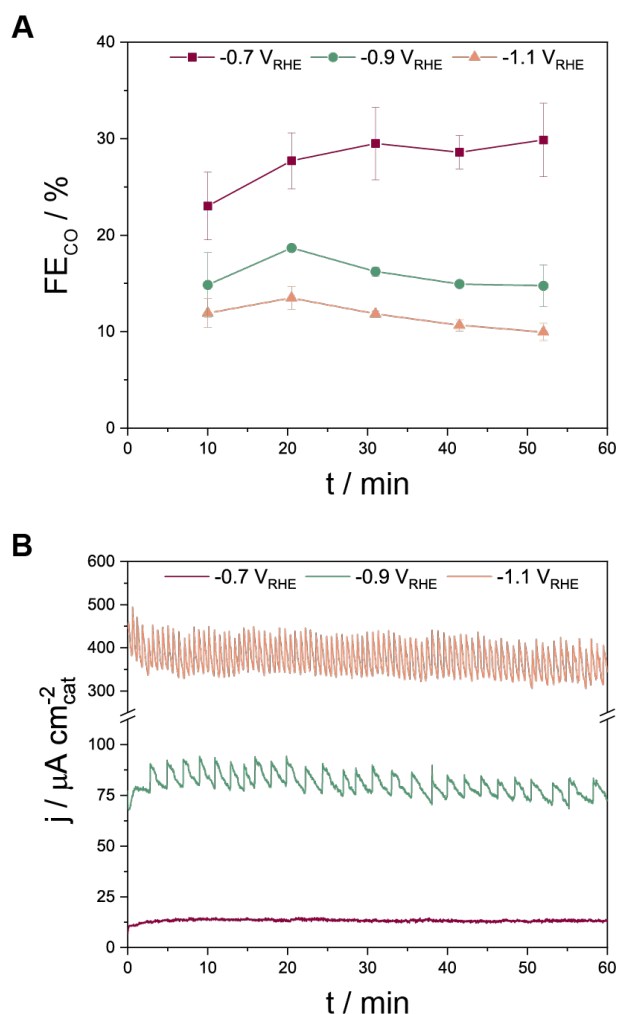
Figure 2. (A) CO FE and (B) total current densities normalized by the area of the Ga NPs (details in the SI) over one hour of CO_2RR in 0.1 M $KHCO_3$ at different applied potentials. Oscillations in current density are attributed to the formation of bubbles.

Investigation of the morphology and surface of the Ga NPs post-electrolysis.

The Pourbaix diagram of Ga in aqueous solution indicates that the gallium oxide skin reduces to metallic Ga at -0.485 V_{RHE}. Also, Ga NPs are liquid at room temperature.[28] Thus, Ga NPs without the oxide skin should rapidly coalesce into bulk metallic gallium at the cathodic potentials applied during CO_2RR. Yet, no visual changes were observed on the electrodes post-electrolysis along with no change in the catalytic performance.

To assess morphological changes of the Ga NPs during electrolysis, we analyzed the electrodes before and after electrolysis at different applied potentials, and the data are summarized in **Figure 3A**. The scanning electron microscopy (SEM) images evidence that the

Ga NPs do remain well-separated from each other during the course of electrolysis. This observation is remarkable because other metal NPs of similar size and under the same conditions undergo tremendous changes and form aggregated structures, sometimes even during the potential ramp.[29,35–37] We note that the size and size distribution of the Ga NPs do increase after electrolysis at the more cathodic voltages (**Figure S5**), however no major coalescence is observed. Even seventy hours of CO_2RR at -0.7 V_{RHE} does not result in noticeable coalescence of Ga NPs (**Figure S6**).

To probe the oxide layer, we performed XPS analysis of the Ga NP electrodes before and after electrolysis at different voltages (**Figure 3B**). First, XPS confirms presence of both the metallic and the oxide components in the as-synthesized Ga NPs. The fitting results indicate that the thickness of oxide layer is *ca.* 2.7 nm (see SI for details and **Table S1**), which agrees well with the results of STEM-EDXS (**Figure 1B-E**). After electrolysis, the oxide contribution decreases, yielding *ca.* 1.6 – 2.3 nm thickness of oxide skin depending on the applied voltage (**Table S1**). We note that the XPS experiment was done *ex situ*, so the electrode surface reoxidizes in the time interval between the release of the cathodic potential and the XPS analysis. Nevertheless, the data clearly indicate that a certain fraction of Ga oxide is reduced during CO_2RR.
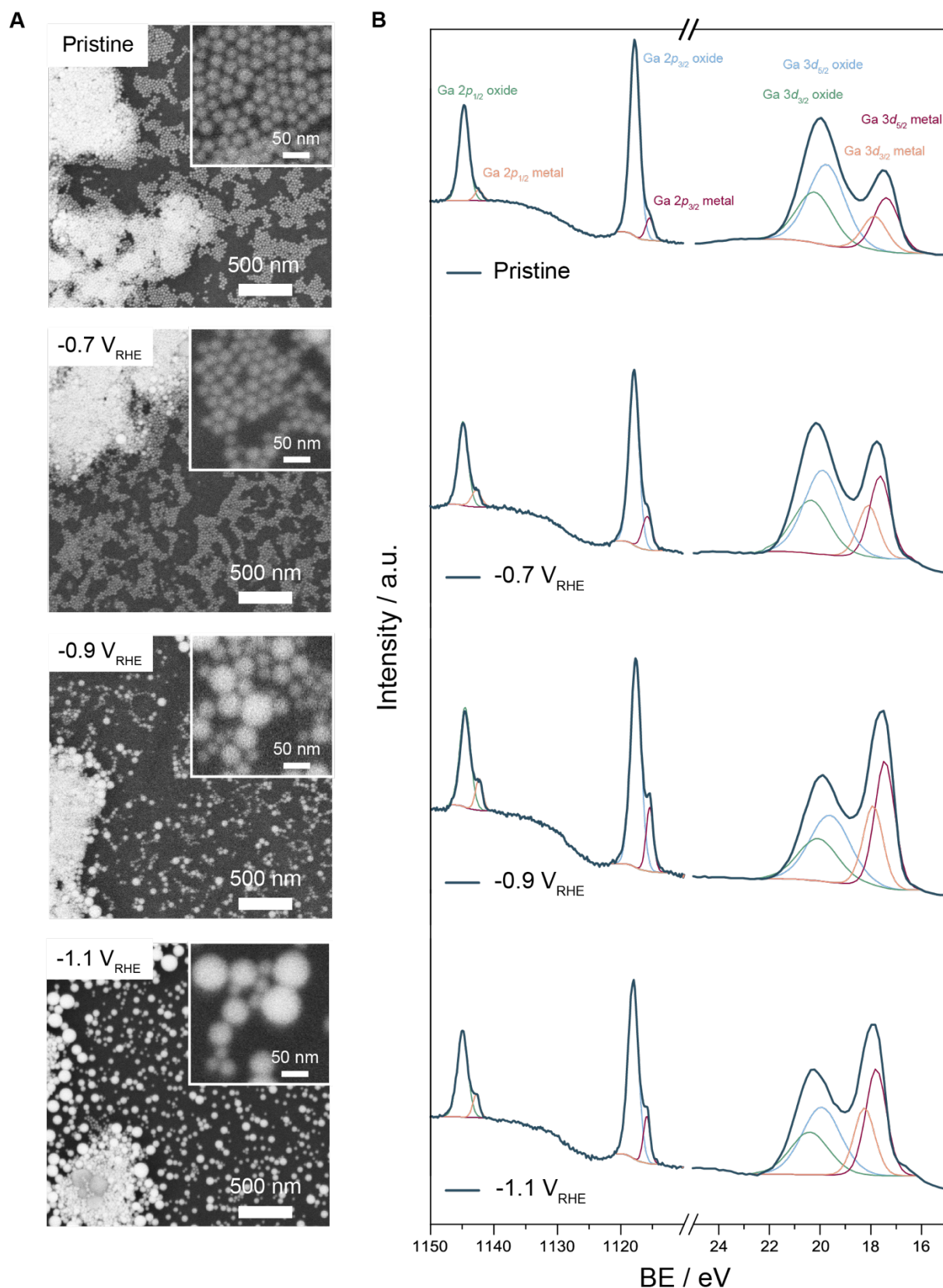
Figure 3. (A) SEM images of Ga NPs electrodes as-prepared and after one hour electrolysis at -0.7 V_{RHE}, -0.9 V_{RHE} and -1.1 V_{RHE}. (B) XPS analysis confirming the presence of the native oxide skin on as-synthesized Ga NPs and Ga NPs after one hour electrolysis at a given

potential. These oxide skin possess a reduced thickness compared to the one of the as-synthesized NPs (**Table S1**).

Transmission electron microscopy characterization.

The melting point of bulk Ga is slightly above room temperature at 29.8 °C.[1] The melting point of Ga NPs is expected to be even lower because of size effects.[38–42] At the same time, unexpected behavior can arise at the nanoscale.[43,44] For example, Ga clusters smaller than 2 nm were predicted to have a higher thermal stability than bigger NPs.[43] One study also reported the thermally stable coexistence of liquid and solid phases in Ga NPs.[44] As the presence of a solid domain in the NPs might explain the absence of rapid coalescence in the Ga NPs, we decided to investigate further the structure of the Ga NPs. Therefore, we performed an *in situ* TEM experiment with heating from cryogenic temperatures back to room temperature.

An interference contrast image along with selected area electron diffraction were recorded at few pre-selected temperatures (**Figure 4**). When cooled to liquid nitrogen temperature, the NPs solidify, which is revealed by visible crystalline planes in the high-resolution images and by the appearance of spots in the electron diffraction. The structure of the NPs corresponds to δ-Ga (**Figure S7**) and confirms that the formation of α-Ga, which is a stable phase in bulk Ga, is suppressed in Ga NPs. The Ga NPs remain crystalline solid at -80 °C, but melt when heated up to -60 °C. However, cooling the NPs back to -80 °C does not result in solidification, which is in line with results reported for supercooling in Ga NPs and hysteresis between their crystallization and melting points.[28,38–40,45]

Altogether, TEM and electron diffraction analysis provide no indication of solid domains being present within the liquid Ga NPs both at ambient and low temperatures. Despite different conditions between cryo-TEM and CO_2RR as well as a different substrate, these findings make the presence of solid domains at operating conditions highly unlikely.
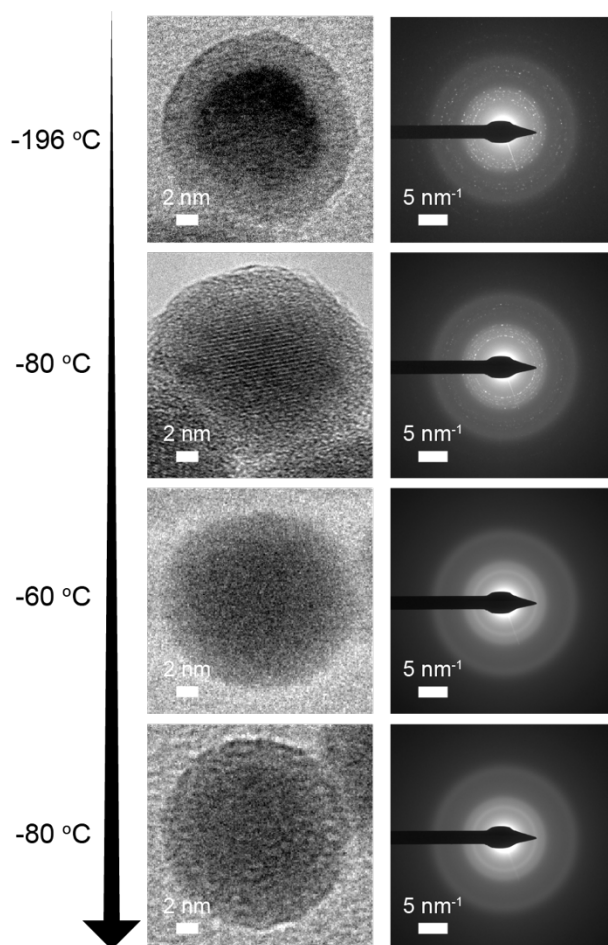
Figure 4. Cryo-TEM (left) and electron diffraction (right) study of Ga NPs at different temperatures: at liquid N_2 temperature (-196 °C), at -80 °C, at -60 °C and again at -80 °C.

Voltammetric characterization.

The electrochemical properties can change when size shrinks to the nanoscale, which is attributed to different electronic configuration or strain effects of the surface.[46,47] Shifts in the redox potentials of the Ga NPs and bulk Ga might explain why Ga NPs do not undergo rapid coalescence.

To assess this possibility, we performed a voltammetric study of Ga NPs in CO_2-saturated 0.1 M $KHCO_3$, which is the electrolyte used for electrochemical CO_2 reduction tests (**Figure 5**). We utilized squared wave voltammetry (SWV), which exhibits enhanced sensitivity compared to a conventional cyclic voltammetry experiment. We selected the testing range in a region where repetitive cycles yield no changes in SWV response (**Figure S8**). The acquired SWV of bulk Ga is shown for the reference. We note that bulk Ga is solid at room temperature, instead the Ga NPs are in their liquid state. To evaluate possible differences

arising from the material physical state, we measured bulk Ga below and above its melting point (at 24 °C and 35 °C, respectively).

The curves of the Ga NPs and of the bulk liquid Ga are qualitatively similar. This result points at the liquid nature of the particles, which is consistent with the TEM in **Figure 4**, and to the absence of size-induced differences in their redox properties. Overall, there are two distinctive features in the investigated potential range: a reduction peak at *ca.* -0.54 V_{RHE} and an oxidation peak at *ca.* -0.51 V_{RHE}. Both values are close to the standard reduction potential of Ga^{3+}/Ga ($E^{\circ}_{Ga_2O_3/Ga} = -0.485\ V_{RHE}$, $E^{\circ}_{GaOOH/Ga} = -0.493\ V_{RHE}$, $E^{\circ}_{Ga(OH)_3/Ga} = -0.415\ V_{RHE}$).[48,49] These numbers agree well with earlier reported investigation of bulk Ga in different electrolytes.[14,50–55] The reduction peak is assigned to the oxide skin, which is followed by steady non-capacitive current increase (assigned to hydrogen evolution reaction and CO$_2$RR) at more negative voltage. The oxidation peak on the reverse scan is attributed to the formation of oxide skin.
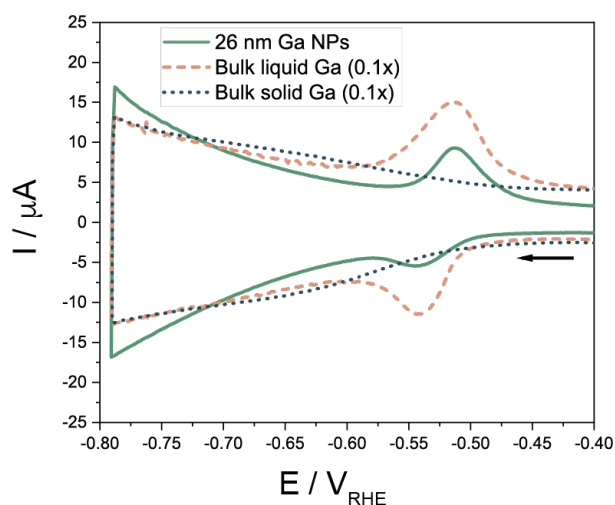

Figure 5. SWV curves of Ga NPs and bulk Ga (in the liquid and solid state) in CO$_2$-saturated 0.1 M KHCO$_3$. The arrow indicates the scan direction.

The solid Ga electrode is distinctly different from the other curves. The observed peaks are broader and shifted *ca.* 0.1 V negative compared to the bulk liquid Ga, in accordance with previous studies.[14,56] The negative shift and peak broadness can be explained by the higher affinity of oxide to solid Ga than to its liquid counterpart.[56] To prove that these differences arise from the difference in the Ga state and are not the direct effect of heating, SWV of Ga

NPs was recorded both at ambient and elevated temperature, showing no significant difference between the two curves (**Figure S9**).

Overall, the voltametric characterization indicates that the oxide skin should be reduced and, thus, the Ga NPs should exist in their liquid metallic state under CO_2RR conditions, which questions the reason for absence of immediate particles coalescence.

***Operando* XAS study of Ga particles during CO_2RR.**

As Ga spontaneously reoxidizes upon air exposure and at open-circuit potential, the only way to probe the presence of the oxide skin during CO_2RR is via *operando* studies. Thus, we performed X-ray Absorption Spectroscopy (XAS) using a cell which reproduces the CO_2RR electrochemical cell (**Figure S10**). **Figure 6** reports the results obtained when the applied potential was -1.1 V_{RHE} as a representative example. We did not observe any difference when operating the electrolyzer at different voltages (**Figure S11**).

The X-ray absorption near edge structure (XANES) map evidenced a fast shift of the Ga absorption edge position towards lower energy when the cathodic voltage is applied (**Figure 6A,B**), which means that the metallic Ga component increases (reference spectra for Ga oxide and metallic Ga are reported in **Figure S12**). This observation agrees well with SWV data indicating the reduction of Ga oxide at -0.54 V_{RHE}, which means that majority of Ga oxide should get reduced at operating voltages. XANES characterization performed with 20 s time resolution indicated that the reduction of the Ga oxide component takes place during the first 2 min of operation and no further changes occur over one hour of electrolysis (**Figure S13**). The XANES spectra at open circuit potential (ocp, i.e. Ga NPs electrode immersed in the electrolyte without applied voltage) and during electrolysis (**Figure 6B)** clearly show the shift of the Ga edge to lower energy when the cathodic voltage is applied. The linear fitting of these curves evidence that the Ga oxide content evolves from 24% to 3% going from ocp to -1.1 V_{RHE}, which correspond to a change in the average oxide thickness from 1.1 nm to *ca.* 0.1 – 0.2 nm (details in the Supporting Information). Chronoamperometry at -1.1 V_{RHE} for 5 hours confirmed that oxidation state of the Ga NPs remains stable after this initial reduction step (**Figure S14**).

Extended X-ray Absorption Fine Structure (EXAFS) analysis provided further insight into the Ga local chemical environment. **Figures 6C** and **S15** indicate a pronounced signal from Ga-O at ocp. When the cathodic voltage is applied, the Ga-O contribution to the signal

decreases, yet it is clearly still present in the EXAFS pattern. Altogether the XANES and EXAFS results are consistent with the presence of roughly a monolayer of Ga oxide on Ga NPs during CO_2RR.
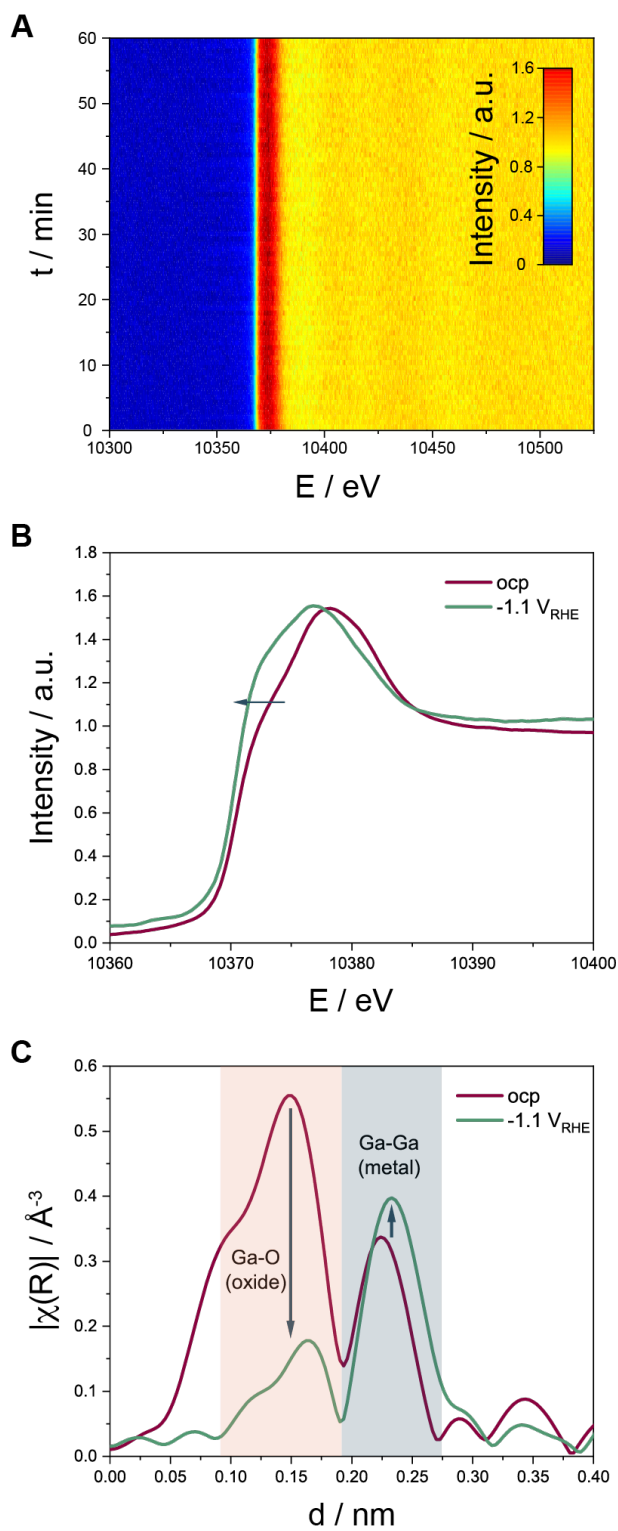
Figure 6. (A) 2D map of XANES spectra during one hour electrolysis at -1.1 V_{RHE}, (B) comparison of the XANES scans at ocp and at -1.1 V_{RHE}, and (C) interatomic distances derived from *operando* EXAFS measurements of Ga NPs at ocp and at -1.1 V_{RHE}. Interatomic distances were not corrected for the phase shift. The red and gray areas indicate distances corresponding to Ga-O and Ga-Ga bonds, respectively.

Mechanistic discussion.

The discovery that Ga oxide is still present under the highly cathodic potential driving CO_2RR is intriguing. Interestingly, this result resembles the residual gallium oxide found in CuGa catalysts under the highly reducing conditions of the thermal CO_2 hydrogenation reaction as long as a few ppm of oxygen were present.[57] Reports by Popova et al. dating back to the 70's claim that even after Ga activation (i.e., at voltages more negative than the reduction peak) a "residual film" of different chemical nature persists on the surface and increases the HER overpotential compared to Ga free of the surface oxide.[58,59] Having acquired this new knowledge, questions regarding the structure and the role of the oxide layer on the Ga NPs during the electrocatalysis arise.

First of all, it is difficult to say whether the oxide of roughly one monolayer thickness is uniformly covering the surface of the Ga NPs or is present in the form of islands on the surface. Both situations are possible.

Second, the oxide layer can be static or dynamic. In the former case, a fraction of the native oxide skin would always be present on the Ga NPs surface during CO_2RR (**Figure 7A**). Herein, CO_2RR could occur on the oxide itself, on the metal surface or at metal/oxide interfacial sites. To gain further insight, we attempted to obtain pure gallium oxide NPs as a reference by electrochemically oxidizing the Ga NPs. However, the current density under the applied potential dramatically decreases with fully oxidized NPs and reliable studies cannot be performed. Furthermore, most of the oxide is reduced back when the cathodic potential is applied, so learning about the CO_2RR reaction of GaO_x NPs is practically impossible.

Alternatively, one can envision the oxide skin to be involved in a dynamic redox cycle where the applied potential reduces it and the coupling with a chemical reaction forms it back (**Figure 7B,C** and Supporting Information for balanced equations). This chemical reaction can be either the reduction of H_2O to H_2 (**Figure 7B**) or the reduction of CO_2 to CO (**Figure 7C**). If the surface oxidation of Ga to GaO_x was coupled with the reduction of H_2O to H_2, the CO_2

reduction to CO would occur on the surface of metallic Ga driven by the applied voltage while H_2 production would result from a chemical step (**Figure 7B**). This mechanism is in qualitative agreement with an earlier study of Ga electrode behavior in alkaline electrolyte with concomitant chemical H_2 evolution.[60] Instead, if the surface oxidation of Ga to GaO_x was coupled directly with the reduction of CO_2 to CO, the negative applied voltage would regenerate the metallic Ga surface and restarts the cycle (**Figure 7C**). This model has been referred to as incipient hydrous oxide adatom mediator (IHOAM) model and it is similar to the mechanism proposed for Ce catalyst dissolved in Galinstan.[13,61]

Whether static or dynamic, the oxide layer during CO_2RR would prevent the rapid coalescence of the Ga NPs. Indeed, even in the case of a dynamic oxide, the surface reoxidation, which is a chemical process, would be faster than particles coalescence, which is a physical phenomenon, thus inhibiting it.[62,63]
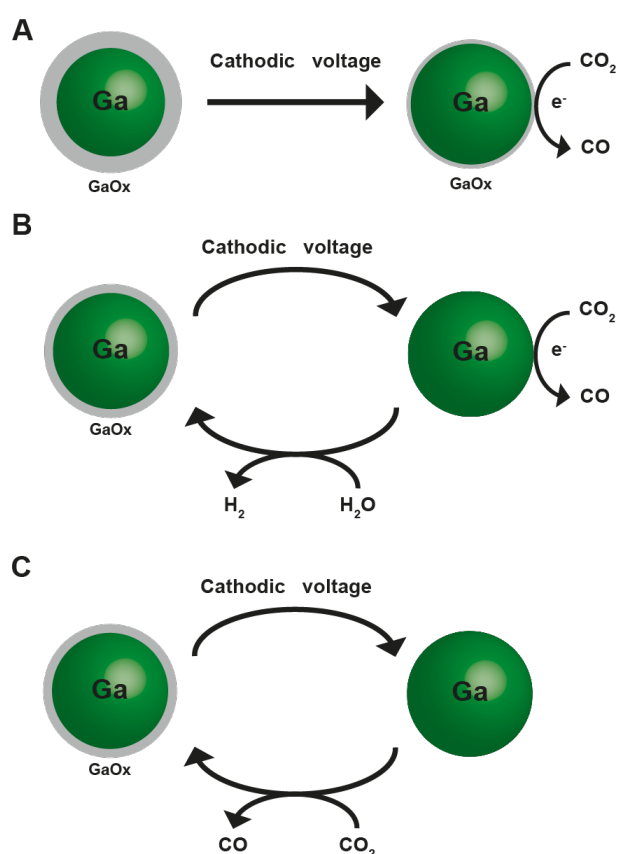

Figure 7. Schematics of possible mechanisms of electrocatalysis on Ga NPs in an aqueous electrolyte, which include (A) a static and (B,C) a dynamic oxide skin. The oxide skin is indicated as GaO_x as its specific stoichiometry is unknown. While the bulk stable oxide phase is Ga_2O_3, earlier studies suggest that Ga(III) oxyhydroxides of mixed compositions may form

as well as unstable Ga species such as Ga(I) (oxy)hydroxides, and even incorporation of anions into the skin is probable.[50,51,59,60]

While we cannot conclude which exact mechanism takes place, we further validated that the oxide is crucial to prevent coalescence of the Ga NPs. For instance, strong metal/support interactions can contribute to anchor nanocatalysts in place and prevent their sintering.[17,18] While the formation of Ga-C bonds is highly unlikely,[64] one can still imagine an interplay between the glassy carbon and the metallic Ga NPs which anchors them during CO_2RR. To test this hypothesis, we chemically removed the oxide skin with acid on the Ga NP electrodes. This treatment resulted in the formation of big Ga agglomerate (**Figure S16**), which eliminates the sole role of the substrate in the prevention of coalescence.

We also found that CO_2 supply and bicarbonate are not essential to prevent coalescence (**Figure S17**), thus the phenomenon appear to be general as far as water is present in the environment. Oxygen dissolved in the electrolyte could contribute to the GaO_x skin retention if the pH is not acidic or alkaline enough to dissolve the shell chemically.

Finally, we demonstrated that the behavior observed for the 26 nm Ga NPs is retained for other sizes (**Figures S18-20**). Smaller (18 nm) and bigger (39 nm) NPs possessed comparable CO_2RR performance and resistance to coalescence. Interestingly, a more pronounced size change with increasing cathodic potential occurs for the bigger NPs. This behavior is counterintuitive as generally coalescence occurs more easily for smaller and more active NPs.[19] Yet, it suggests that the lower surface to volume ratio of the bigger NPs makes the oxide skin protection less effective. To provide further insight on the size dependent behavior, we attempted to study micron-size Ga particles, however their broad size distribution prevented us to draw reliable conclusions (**Figure S21**).

Conclusions

We have demonstrated that Ga NPs can be implemented as liquid metal catalysts for the electrochemical CO_2RR while preserving the nanoparticles morphology. Based on *operando* XAS, we propose an oxide-mediated retarded coalescence mechanism wherein the native oxide skin persists during CO_2RR in a static or dynamic fashion.

This discovery is significant because the same oxide-mediated retarded coalescence mechanism can be conceived for other Ga-based alloys and intermetallics, many of which have been predicted as promising electrocatalysts for different reactions, including CO2RR[65,66]. By exploiting colloidal chemistry, which allows the synthesis of well-defined NPs with tunable compositions,[27,67] we envision a library of LM NPs to emerge as a new class of electrocatalysts which are active, selective and coalescence-resistant.

References

(1) Daeneke, T.; Khoshmanesh, K.; Mahmood, N.; De Castro, I. A.; Esrafilzadeh, D.; Barrow, S. J.; Dickey, M. D.; Kalantar-Zadeh, K. Liquid Metals: Fundamentals and Applications in Chemistry. *Chem. Soc. Rev.* **2018**, *47*, 4073–4111.

(2) Song, H.; Kim, T.; Kang, S.; Jin, H.; Lee, K.; Jae Yoon, H.; Song, H.; Kim, T.; Kang, S.; Jin, H.; Lee, K.; Yoon, H. J. Ga-Based Liquid Metal Micro/Nanoparticles: Recent Advances and Applications. *Small* **2020**, *16*, 1903391.

(3) Kalantar-Zadeh, K.; Rahim, M. A.; Tang, J. Low Melting Temperature Liquid Metals and Their Impacts on Physical Chemistry. *Accounts Mater. Res.* **2021**, *2*, 577–580.

(4) Tang, S. Y.; Tabor, C.; Kalantar-Zadeh, K.; Dickey, M. D. Gallium Liquid Metal: The Devil's Elixir. *Annu. Rev. Mater. Res.* **2021**, *51*, 381–408.

(5) Kalantar-Zadeh, K.; Tang, J.; Daeneke, T.; O'Mullane, A. P.; Stewart, L. A.; Liu, J.; Majidi, C.; Ruoff, R. S.; Weiss, P. S.; Dickey, M. D. Emergence of Liquid Metals in Nanotechnology. *ACS Nano* **2019**, *13*, 7388–7395.

(6) Zuraiqi, K.; Zavabeti, A.; Allioux, F. M.; Tang, J.; Nguyen, C. K.; Tafazolymotie, P.; Mayyas, M.; Ramarao, A. V.; Spencer, M.; Shah, K.; McConville, C. F.; Kalantar-Zadeh, K.; Chiang, K.; Daeneke, T. Liquid Metals in Catalysis for Energy Applications. *Joule* **2020**, *4*, 2290–2321.

(7) Martin, A.; Du, C.; Chang, B.; Thuo, M. Complexity and Opportunities in Liquid Metal Surface Oxides. *Chem. Mater.* **2020**, *32*, 9045–9055.

(8) Crook, J.; Mousavi, A. The Chlor-Alkali Process: A Review of History and Pollution. *Environ. Forensics* **2016**, *17*, 211–217.

(9) Taccardi, N.; Grabau, M.; Debuschewitz, J.; Distaso, M.; Brandl, M.; Hock, R.; Maier, F.; Papp, C.; Erhard, J.; Neiss, C.; Peukert, W.; Görling, A.; Steinrück, H. P.; Wasserscheid, P. Gallium-Rich Pd–Ga Phases as Supported Liquid Metal Catalysts. *Nat. Chem.* **2017**, *9*, 862–867.

(10) Upham, D. C.; Agarwal, V.; Khechfe, A.; Snodgrass, Z. R.; Gordon, M. J.; Metiu, H.; McFarland, E. W. Catalytic Molten Metals for the Direct Conversion of Methane to Hydrogen and Separable Carbon. *Science* **2017**, *358*, 917–921.

(11) Raman, N.; Maisel, S.; Grabau, M.; Taccardi, N.; Debuschewitz, J.; Wolf, M.; Wittkämper, H.; Bauer, T.; Wu, M.; Haumann, M.; Papp, C.; Görling, A.; Spiecker, E.; Libuda, J.; Steinrück, H. P.; Wasserscheid, P. Highly Effective Propane Dehydrogenation Using Ga-Rh Supported Catalytically Active Liquid Metal Solutions.

ACS Catal. **2019**, *9*, 9499–9507.

(12) Palmer, C.; Upham, D. C.; Smart, S.; Gordon, M. J.; Metiu, H.; McFarland, E. W. Dry Reforming of Methane Catalysed by Molten Metal Alloys. *Nat. Catal.* **2020**, *3*, 83–89.

(13) Esrafilzadeh, D.; Zavabeti, A.; Jalili, R.; Atkin, P.; Choi, J.; Carey, B. J.; Brkljača, R.; O'Mullane, A. P.; Dickey, M. D.; Officer, D. L.; MacFarlane, D. R.; Daeneke, T.; Kalantar-Zadeh, K. Room Temperature CO2 Reduction to Solid Carbon Species on Liquid Metals Featuring Atomically Thin Ceria Interfaces. *Nat. Commun.* **2019**, *10*, 1–8.

(14) Liu, H.; Xia, J.; Zhang, N.; Cheng, H.; Bi, W.; Zu, X.; Chu, W.; Wu, H. A.; Wu, C.; Xie, Y. Solid–Liquid Phase Transition Induced Electrocatalytic Switching from Hydrogen Evolution to Highly Selective CO2 Reduction. *Nat. Catal.* **2021**, *4*, 202–211.

(15) Allioux, F. M.; Merhebi, S.; Tang, J.; Idrus-Saidi, S. A.; Abbasi, R.; Saborio, M. G.; Ghasemian, M. B.; Han, J.; Namivandi-Zangeneh, R.; O'Mullane, A. P.; Koshy, P.; Daiyan, R.; Amal, R.; Boyer, C.; Kalantar-Zadeh, K. Catalytic Metal Foam by Chemical Melting and Sintering of Liquid Metal Nanoparticles. *Adv. Funct. Mater.* **2020**, *30*, 1907879.

(16) Tang, J.; Daiyan, R.; Ghasemian, M. B.; Idrus-Saidi, S. A.; Zavabeti, A.; Daeneke, T.; Yang, J.; Koshy, P.; Cheong, S.; Tilley, R. D.; Kaner, R. B.; Amal, R.; Kalantar-Zadeh, K. Advantages of Eutectic Alloys for Creating Catalysts in the Realm of Nanotechnology-Enabled Metallurgy. *Nat. Commun.* **2019**, *10*, 1–14.

(17) Guntern, Y. T.; Okatenko, V.; Pankhurst, J.; Varandili, S. B.; Iyengar, P.; Koolen, C.; Stoian, D.; Vavra, J.; Buonsanti, R. Colloidal Nanocrystals as Electrocatalysts with Tunable Activity and Selectivity. *ACS Catal.* **2021**, *11*, 1248–1295.

(18) Cargnello, M. Colloidal Nanocrystals as Building Blocks for Well-Defined Heterogeneous Catalysts. *Chem. Mater.* **2019**, *31*, 576–596.

(19) Goodman, E. D.; Schwalbe, J. A.; Cargnello, M. Mechanistic Understanding and the Rational Design of Sinter-Resistant Heterogeneous Catalysts. *ACS Catal.* **2017**, *7*, 7156–7173.

(20) Otor, H. O.; Steiner, J. B.; García-Sancho, C.; Alba-Rubio, A. C. Encapsulation Methods for Control of Catalyst Deactivation: A Review. *ACS Catal.* **2020**, *10*, 7630–7656.

(21) Zhang, W.; Ou, J. Z.; Tang, S.-Y.; Sivan, V.; Yao, D. D.; Latham, K.; Khoshmanesh, K.; Mitchell, A.; O'Mullane, A. P.; Kalantar-zadeh, K. Liquid Metal/Metal Oxide

Frameworks. *Adv. Funct. Mater.* **2014**, *24*, 3799–3807.

(22) Idrus-Saidi, S. A.; Tang, J.; Ghasemian, M. B.; Yang, J.; Han, J.; Syed, N.; Daeneke, T.; Abbasi, R.; Koshy, P.; O'Mullane, A. P.; Kalantar-Zadeh, K. Liquid Metal Core– Shell Structures Functionalised via Mechanical Agitation: The Example of Field's Metal. *J. Mater. Chem. A* **2019**, *7*, 17876–17887.

(23) Nitopi, S.; Bertheussen, E.; Scott, S. B.; Liu, X.; Engstfeld, A. K.; Horch, S.; Seger, B.; Stephens, I. E. L.; Chan, K.; Hahn, C.; Nørskov, J. K.; Jaramillo, T. F.; Chorkendorff, I. Progress and Perspectives of Electrochemical CO2 Reduction on Copper in Aqueous Electrolyte. *Chem. Rev.* **2019**, *119*, 7610–7672.

(24) Ross, M. B.; De Luna, P.; Li, Y.; Dinh, C. T.; Kim, D.; Yang, P.; Sargent, E. H. Designing Materials for Electrochemical Carbon Dioxide Recycling. *Nat. Catal.* **2019**, *2*, 648–658.

(25) Hori, Y.; Wakebe, H.; Tsukamoto, T.; Koga, O. Electrocatalytic Process of CO Selectivity in Electrochemical Reduction of CO2 at Metal Electrodes in Aqueous Media. *Electrochim. Acta* **1994**, *39*, 1833–1839.

(26) Yan, C.; Lin, L.; Gao, D.; Wang, G.; Bao, X. Selective CO2 Electroreduction over an Oxide-Derived Gallium Catalyst. *J. Mater. Chem. A* **2018**, *6*, 19743–19749.

(27) Castilla-Amoros, L.; Stoian, D.; Pankhurst, J.; Varandili, S.; Buonsanti, R. Exploring the Chemical Reactivity of Gallium Liquid Metal Nanoparticles in Galvanic Replacement. *J. Am. Chem. Soc.* **2020**, *142*, 19283–19290.

(28) Yarema, M.; Wörle, M.; Rossell, M. D.; Erni, R.; Caputo, R.; Protesescu, L.; Kravchyk, K. V.; Dirin, D. N.; Lienau, K.; Von Rohr, F.; Schilling, A.; Nachtegaal, M.; Kovalenko, M. V. Monodisperse Colloidal Gallium Nanoparticles: Synthesis, Low Temperature Crystallization, Surface Plasmon Resonance and Li-Ion Storage. *J. Am. Chem. Soc.* **2014**, *136*, 12422–12430.

(29) Vavra, J.; Shen, T.-H.; Stoian, D.; Tileli, V.; Buonsanti, R. Real-time Monitoring Reveals Dissolution/Redeposition Mechanism in Cu Nanocatalysts during the Initial Stages of the CO2 Reduction Reaction. *Angew. Chemie Int. Ed.* **2021**, *60*, 1347–1354.

(30) Varandili, S. B.; Stoian, D.; Vavra, J.; Rossi, K.; Pankhurst, J. R.; Guntern, Y. T.; López, N.; Buonsanti, R. Elucidating the Structure-Dependent Selectivity of CuZn towards Methane and Ethanol in CO2 Electroreduction Using Tailored Cu/ZnO Precatalysts. *Chem. Sci.* **2021**, *12*, 14484–14493.

(31) Ravel, B.; Newville, M. ATHENA, ARTEMIS, HEPHAESTUS: Data Analysis for X-Ray Absorption Spectroscopy Using IFEFFIT. *J. Synchrotron Radiat.* **2005**, *12*, 537–

541.

(32)   Castilla-Amorós, L.; Chien, T. C. C.; Pankhurst, J. R.; Buonsanti, R. Modulating the Reactivity of Liquid Ga Nanoparticle Inks by Modifying Their Surface Chemistry. *J. Am. Chem. Soc.* **2022**, *144*, 1993–2001.

(33)   Peng, X. D.; Wang, A. W.; Toseland, B. A.; Tijm, P. J. A. Single-Step Syngas-to-Dimethyl Ether Processes for Optimal Productivity, Minimal Emissions, and Natural Gas-Derived Syngas. *Ind. Eng. Chem. Res.* **1999**, *38*, 4381–4388.

(34)   Ciferno, J. P.; Marano, J. J. *Benchmarking Biomass Gasification Technologies for Fuels, Chemicals and Hydrogen Production*; 2009.

(35)   Kim, D.; Kley, C. S.; Li, Y.; Yang, P. Copper Nanoparticle Ensembles for Selective Electroreduction of CO2 to C2–C3 Products. *Proc. Natl. Acad. Sci. U. S. A.* **2017**, *114*, 10560–10565.

(36)   Manthiram, K.; Surendranath, Y.; Alivisatos, A. P. Dendritic Assembly of Gold Nanoparticles during Fuel-Forming Electrocatalysis. *J. Am. Chem. Soc.* **2014**, *136*, 7237–7240.

(37)   Guntern, Y. T.; Pankhurst, J. R.; Vávra, J.; Mensi, M.; Mantella, V.; Schouwink, P.; Buonsanti, R. Nanocrystal/Metal–Organic Framework Hybrids as Electrocatalytic Platforms for CO_2 Conversion. *Angew. Chemie Int. Ed.* **2019**, *58*, 12632–12639.

(38)   Chen, X. M.; Fei, G. T.; Zheng, K. The Solid State Phase Transition of Gallium Particles and Its Size Dependence. *J. Phys. Condens. Matter* **2009**, *21*, 245403.

(39)   Di Cicco, A. Phase Transitions in Confined Gallium Droplets. *Phys. Rev. Lett.* **1998**, *81*, 2942–2945.

(40)   Zheludev, N. Single Nanoparticle as Photonic Switch and Optical Memory Element. *J. Opt. A Pure Appl. Opt.* **2006**, *8*, S1.

(41)   Ghigna, P.; Spinolo, G.; Parravicini, G. B.; Stella, A.; Migliori, A.; Kofman, R. Metallic versus Covalent Bonding: Ga Nanoparticles as a Case Study. *J. Am. Chem. Soc.* **2007**, *129*, 8026–8033.

(42)   He, H.; Fei, G. T.; Cui, P.; Zheng, K.; Liang, L. M.; Li, Y.; De Zhang, L. Relation between Size and Phase Structure of Gallium: Differential Scanning Calorimeter Experiments. *Phys. Rev. B* **2005**, *72*, 073310.

(43)   Breaux, G. A.; Hillman, D. A.; Neal, C. M.; Benirschke, R. C.; Jarrold, M. F. Gallium Cluster "Magic Melters." *J. Am. Chem. Soc.* **2004**, *126*, 8628–8629.

(44)   Losurdo, M.; Suvorova, A.; Rubanov, S.; Hingerl, K.; Brown, A. S. Thermally Stable Coexistence of Liquid and Solid Phases in Gallium Nanoparticles. *Nat. Mater.* **2016**,

15, 995–1002.

(45) Borisov, B. F.; Charnaya, E. V.; Hoffmann, W. D.; Michel, D.; Shelyapin, A. V.; Kumzerov, Y. A. Nuclear Magnetic Resonance and Acoustic Investigations of the Melting - Freezing Phase Transition of Gallium in a Porous Glass. *J. Phys. Condens. Matter* **1997**, *9*, 3377–3386.

(46) Reier, T.; Oezaslan, M.; Strasser, P. Electrocatalytic Oxygen Evolution Reaction (OER) on Ru, Ir, and Pt Catalysts: A Comparative Study of Nanoparticles and Bulk Materials. *ACS Catal.* **2012**, *2*, 1765–1772.

(47) Ma, H.; Gao, P.; Qian, P.; Su, Y. Size-Dependent Electrochemical Properties of Pure Metallic Nanoparticles. *J. Phys. Chem. C* **2020**, *124*, 3403–3409.

(48) Pourbaix, M. *Atlas of Electrochemical Equilibria in Aqueous Solutions*, 2nd ed.; National Association of Corrosion Engineers: Houston, 1966.

(49) Bratsch, S. G. Standard Electrode Potentials and Temperature Coefficients in Water at 298.15 K. *J. Phys. Chem. Ref. Data* **1989**, *18*, 1–21.

(50) Korshunov, V. N. Behaviour of Rotating Disk Ga-Anode in Alkaline Environment. *Elektrokhimiya* **1995**, *31*, 1122–1136.

(51) Korshunov, V. N.; Safonov, V. A. Behavior of Gallium Anodes in Carbonate Buffer Solutions. *Russ. J. Electrochem.* **2001**, *37*, 1089–1095.

(52) Korshunov, V. N.; Safonov, V. A. Electroreduction of Peroxodisulfate Anions as a Probe Reaction for Studying Passivation of Solid Gallium in Sulfate Media. *Russ. J. Electrochem.* **2002**, *38*, 768–774.

(53) Varadharaj, A.; Prabhakara Rao, G. Cyclic Voltammetric Studies on Gallium Film Electrodes in Alkaline Media. *Proc. Indian Acad. Sci. - Chem. Sci.* **1990**, *102*, 177–187.

(54) Mayyas, M.; Kalantar-Zadeh, K.; Mousavi, M.; Ghasemian, M. B.; Abbasi, R.; Li, H.; Christoe, M. J.; Han, J.; Wang, Y.; Zhang, C.; Rahim, M. A.; Tang, J.; Yang, J.; Esrafilzadeh, D.; Jalili, R.; Allioux, F. M.; O'Mullane, A. P. Pulsing Liquid Alloys for Nanomaterials Synthesis. *ACS Nano* **2020**, *14*, 14070–14079.

(55) Chung, Y.; Lee, C.-W. Electrochemistry of Gallium. *J. Electrochem. Sci. Technol.* **2013**, *4*, 1–18.

(56) Popova, T. I.; Simonova, N. A.; Moyseeva, Z. J.; Bardina, N. G. Formation of Passivating Films on Ga in Aqueous Electrolytes I. *Elektrokhimiya* **1970**, *6*, 706–708.

(57) Zhong, J. Q.; Shaikhutdinov, S.; Roldan Cuenya, B. Structural Evolution of Ga-Cu Model Catalysts for CO2Hydrogenation Reactions. *J. Phys. Chem. C* **2021**, *125*, 1361–

1367.

(58)   Popova, T. I.; Simonova, N. A.; Moyseeva, Z. J.; Bardina, N. G. Formation of Passivating Films on Ga in Aqueous Electrolytes II. *Elektrokhimiya* **1970**, *6*, 1125–1128.

(59)   Popova, T. I.; Timofeeva, L. Z.; Simonova, N. A.; Bardina, N. G. Influence of F- Ions Adsorption on Passive Ga Dissolution. *Elektrokhimiya* **1975**, *11*, 1430–1432.

(60)   Selekhova, N. P.; Lyubimova, N. A.; Leikis, D. I. Anodic Dissolution of Ga in Alkaline Gallate Electrolytes. *Elektrokhimiya* **1972**, *8*, 721–723.

(61)   Burke, L. D. An Interfacial Mediator Interpretation of Noble Metal Electrocatalysis. *Platin. Met. Rev.* **1994**, *38*, 166–173.

(62)   Cheek, Q.; Fahrenkrug, E.; Hlynchuk, S.; Alsem, D. H.; Salmon, N. J.; Maldonado, S. In Situ Transmission Electron Microscopy Measurements of Ge Nanowire Synthesis with Liquid Metal Nanodroplets in Water. *ACS Nano* **2020**, *14*, 2869–2879.

(63)   Kalz, K. F.; Kraehnert, R.; Dvoyashkin, M.; Dittmeyer, R.; Gläser, R.; Krewer, U.; Reuter, K.; Grunwaldt, J. D. Future Challenges in Heterogeneous Catalysis: Understanding Catalysts under Dynamic Reaction Conditions. *ChemCatChem* **2017**, *9*, 17–29.

(64)   Kumar, V. B.; Monte, M.; Mathon, O.; Pascarelli, S.; Porat, Z.; Gedanken, A. The Interaction between Molten Gallium and the Hydrocarbon Medium Induced by Ultrasonic Energy—Can Gallium Carbide Be Formed? *J. Am. Ceram. Soc.* **2017**, *100*, 3305–3315.

(65)   Tran, K.; Ulissi, Z. W. Active Learning across Intermetallics to Guide Discovery of Electrocatalysts for CO2 Reduction and H2 Evolution. *Nat. Catal.* **2018**, *1*, 696–703.

(66)   Zhong, M.; Tran, K.; Min, Y.; Wang, C.; Wang, Z.; Dinh, C. T.; De Luna, P.; Yu, Z.; Rasouli, A. S.; Brodersen, P.; Sun, S.; Voznyy, O.; Tan, C. S.; Askerka, M.; Che, F.; Liu, M.; Seifitokaldani, A.; Pang, Y.; Lo, S. C.; Ip, A.; Ulissi, Z.; Sargent, E. H. Accelerated Discovery of CO2 Electrocatalysts Using Active Machine Learning. *Nature* **2020**, *581*, 178–183.

(67)   Clarysse, J.; Moser, A.; Yarema, O.; Wood, V.; Yarema, M. Size- and Composition-Controlled Intermetallic Nanocrystals via Amalgamation Seeded Growth. *Sci. Adv.* **2021**, *7*, eabg1934.